Journal of Materials Chemistry C

ROYAL SOCIETY OF CHEMISTRY

PAPER

View Article Online
View Journal | View Issue

Cite this: J. Mater. Chem. C, 2020, 8, 15119

"Heavy-atom effects" in the parent [1]benzochalcogenopheno[3,2-*b*][1]benzochalcogenophene system†

Chengyuan Wang, [a] Mamatimin Abbas, [b] Guillaume Wantz, [b] Kohsuke Kawabata [ac] and Kazuo Takimiya *[ac]

[1]Benzochalcogenopheno[3,2-*b*][1]benzochalcogenophenes (BXBXs) have been the key π-conjugated core structures in the development of superior organic semiconductors for organic field-effect transistors (OFETs). The semiconducting properties of parent BXBXs, however, have not been well examined. In this work, we focus on the parent system and investigate the effect of different chalcogen atoms, *i.e.*, sulphur, selenium or tellurium atoms, in the BXBX core on molecular electronic properties, crystal structures, intermolecular interactions, solid-state electronic structures, and carrier transport properties. Replacing the sulphur atoms in [1]benzothieno[3,2-*b*][1]benzothiophene (**BTBT**) with selenium atoms marginally changes the molecular properties and the intermolecular interactions, thus resulting in similar herringbone packing structures in the solid state. The carrier mobilities of single-crystal (SC)-OFETs are higher for [1]benzoselenopheno[3,2-*b*][1]benzoselenophene (**BSBS**) than those for **BTBT**, which can be understood by the increase in the intermolecular electronic coupling in **BSBS**, originating from the larger atomic radius and more diffused electron cloud of selenium atoms than sulphur atoms. On the other hand, the packing structure of [1]benzotelluropheno[3,2-*b*][1]benzotellurophene (**BTeBTe**) is determined to be a dimeric herringbone structure. The crystal structure of **BTeBTe** being strikingly different from those of **BTBT** and **BSBS** can be explained by a drastic change in the intermolecular interaction in the solid state. Furthermore, the **BTeBTe**-based SC-OFETs do not show transistor response. To elucidate these unexpected results, various experimental and theoretical approaches, *e.g.*, evaluation of ionization potentials and band calculations, are examined. Through these approaches, a comprehensive view of the parent BXBX system is given, and also both the pros and cons of incorporation of heavy chalcogen atoms, positive and negative "heavy-atom effects", in developing organic semiconductors are discussed.

Received 19th March 2020,
Accepted 11th May 2020

DOI: 10.1039/d0tc01408g

rsc.li/materials-c

Introduction

Large acenes and heteroacenes have been widely utilized as the active semiconducting material in organic field-effect transistors (OFETs) in the past decades.[1–3] Thienoacenes that combine the structural features of acenes and thiophenes have been an important family of heteroacenes exhibiting promising carrier transport properties.[4,5] [1]Benzochalcogenopheno[3,2-*b*][1]benzochalcogenophenes (BXBXs, Fig. 1) are among the most important and frequently used π-core structures for the development of superior organic semiconductors.[6] In particular, the sulphur analogue, [1]benzothieno[3,2-*b*][1]benzothiophene (**BTBT**, Fig. 1), has afforded air-stable, high-performance organic semiconductors, *e.g.*, symmetric[7,8] and asymmetric derivatives[9] with various substituents, such as phenyl or alkyl groups at the 2,7-positions[10] or aromatic-fused derivatives[11,12] acting as excellent active-layer materials in OFETs *via* vapour- or solution-processes. A remarkable example is 2,7-dioctyl-**BTBT** (C_8-**BTBT**), which was reported to give the highest hole mobilities in OFETs with solution-deposited thin films.[13,14]

In contrast to these fruitful results on BXBX derivatives as organic semiconductors, the parent system, unsubstituted BXBXs, has been rarely examined as the active material in OFETs.[15] This prompted us to evaluate the semiconducting properties of the parent BXBX molecules. Furthermore, as the BXBX core has two chalcogenophene rings out of four aromatic rings, the parent system would be an ideal platform to elucidate the so-called

[a] *Emergent Molecular Function Research Team, RIKEN Center for Emergent Matter Science (CEMS), 2-1 Hirosawa, Wako, Saitama 351-0198, Japan. E-mail: takimiya@riken.jp*
[b] *Univ. Bordeaux, IMS, CNRS, UMR-5218, Bordeaux INP, ENSCBP, 33405 Talence, France*
[c] *Department of Chemistry, Graduate School of Science, Tohoku University, 6-3 Aoba, Aramaki, Aoba-ku, Sendai, Miyagi 980-8578, Japan*

† Electronic supplementary information (ESI) available. CCDC 1908813. For ESI and crystallographic data in CIF or other electronic format see DOI: 10.1039/d0tc01408g

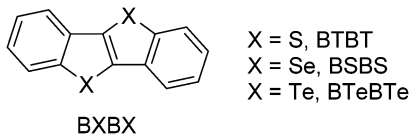

BXBX

Fig. 1 Molecular structures of the parent BXBXs.

"heavy-atom effects", the effects on the structure and properties that are caused by replacing the sulphur atoms in **BTBT** with selenium or tellurium atoms. The heavy atoms are believed to improve the semiconducting properties of the thienoacenes, owing to their large atomic radius, high polarizability, and diffused electron clouds, which are assumed to bring more efficient intermolecular electronic coupling in the solid state.[16–19] In fact, several approaches to take advantage of the heavy-atom effects in BXBX derivatives have been examined.[20–22] However, the existence of substituents, *e.g.*, alkyl groups, makes it difficult to clarify the effects caused by the selenium atoms incorporated.

With these interests, we carried out systematic studies on parent BXBXs with sulphur, selenium, and tellurium atoms (Fig. 1), in terms of molecular electronic properties, packing structures in the solid state, intermolecular electronic couplings, and carrier transport properties of single-crystal OFETs (SC-OFETs).

Experimental

Synthesis of materials

Parent **BTBT**,[23] **BSBS**,[21] and **BTeBTe**[24] were synthesized based on the reported procedures. The materials were purified by multiple train-sublimation before device fabrication.

Device fabrication and characterization

The single crystals of the BXBXs were grown by a physical vapour transport (PVT) method with argon as the carrier gas.[25] The SC-OFETs were fabricated in a bottom-gate top-contact (BGTC) device configuration with SiO_2 as the dielectric layer, or a top-gate top-contact (TGTC) device configuration with parylene C as the dielectric layer, respectively (Fig. S1, ESI†). To fabricate the BGTC SC-OFETs, free-standing single-crystals were laminated on an octadecyltrichlorosilane (ODTS)-modified, heavily doped n^+-Si (100) wafer with 200 nm thermally grown SiO_2 (C_i = 17.3 nF cm^{-2}). On top of the single crystals, colloidal graphite suspended in water was painted as source and drain electrodes.[26] To fabricate the TGTC SC-OFETs, ~500 nm parylene C films (ε = 3.15; C_i was calculated based on the exact thickness of the parylene C film, which was ~5 nF cm^{-2}) were deposited on the single crystals with the source and drain electrodes on the substrate by a chemical vapour deposition (CVD) technique. On top of the parylene C films colloidal graphite was painted as the gate electrode. The channel length (L) and width (W) of the SC-OFETs were optically determined under a microscope. The devices were characterized at room temperature under ambient conditions with a Keithley 4200 semiconducting parameter analyser. Field-effect mobility (μ) was calculated in the saturation regime using the following eqn (1):

$$I_D = C_i\mu(W/2L)(V_G - V_{th})^2 \quad (1)$$

where C_i is the total capacitance of the SiO_2 modified with ODTS or the parylene C film. V_G and V_{th} are the gate and threshold voltages, respectively.

Theoretical calculations

The geometries of isolated molecules in the neutral and cationic states were optimized using the (U)B3LYP/3-21g or (U)B3LYP/6-31g(d) level with the Gaussian 16 program package.[27] Note that the 6-31g(d) basis set does not cover tellurium atoms, and thus the 3-21g basis set was used for the calculations. For **BTBT** and **BSBS**, calculations at the (U)B3LYP/6-31g(d) level of theory were also carried out. The results were almost identical with those obtained with (U)B3LYP/3-21g (Fig. S2 and S3, ESI†). The reorganization energy (λ) of the molecules was calculated by using the adiabatic potential energy surface method in eqn (2):

$$\lambda = \lambda_0 + \lambda_+ = (E_0^* - E_0) + (E_+^* - E_+) \quad (2)$$

where E_0^*, E_0, E_+^*, and E_+ represent the energies of a neutral molecule in the cationic geometry, a neutral molecule in the optimized geometry, a cationic molecule in the neutral geometry, and a cationic molecule in the optimized geometry, respectively.[28]

Intermolecular electronic coupling (transfer integral, t) in different molecular dimers extracted from the single-crystal structures was calculated with the Amsterdam Density Functional (ADF) program.[29] With λ_s and t_s, anisotropic theoretical mobilities were calculated according to the reported procedure as described in the ESI.†[30,31]

Hirshfeld surfaces were computed using the CrystalExplore 17.5 program to visualize intermolecular contacts in the crystalline state.[32,33] Intermolecular interaction energies for the dimers of **BTBT** and **BSBS** extracted from the crystal structures were calculated by symmetry-adapted perturbation theory (SAPT) calculations with the jun-cc-pVDZ level using the PSI4 program package.[34,35] Band structure calculations were carried out with the Crystal17 program at the B3LYP/3-21g level of theory using a 4 × 4 × 4 k-point Pack–Monkhorst net, with the geometry of **BTBT**, **BSBS**, and **BTeBTe** determined by single crystal X-ray analysis.[36] The carrier effective masses were evaluated by parabolic-fitting at the band extrema (Γ–Y direction).[37]

Results

Physicochemical properties of BXBXs

Fig. 2a shows the UV-Vis absorption spectra of the BXBXs in chloroform. **BTBT** and **BSBS** have similar absorption bands, the latter of which are slightly red-shifted; the on-set of absorption for **BSBS** is 356 nm, which corresponds to an optical bandgap (E_g) of 3.48 eV, whereas those for BTBT are 342 nm and 3.63 eV, respectively. In the cyclic voltammograms (CVs) in benzonitrile solution (Fig. 2b), **BTBT** and **BSBS** show one reversible or irreversible oxidation peak, respectively. The onsets of the oxidation peaks (E_{onset}^{OX}) of **BTBT** and **BSBS** are 0.93 and 0.80 V *versus* Fc^+/Fc, respectively, which correspond to the HOMO energy levels of −5.73 and −5.60 eV, respectively. The similarities of **BTBT** and **BSBS** in the absorption spectra and CVs suggest that the

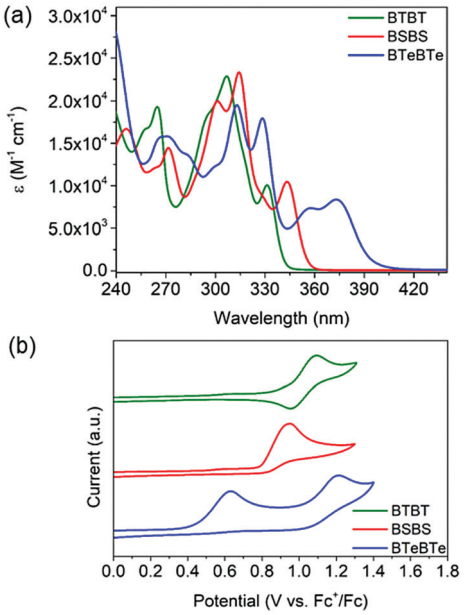

Fig. 2 (a) UV-vis absorption spectra in the chloroform solution and (b) cyclic voltammograms in the benzonitrile solution of **BTBT**, **BSBS**, and **BTeBTe**.

substitution of sulphur with selenium atoms marginally influences the electronic structure of the molecules (Table 1).

In contrast, the absorption spectrum and CV of **BTeBTe** are remarkably different from those of **BTBT** and **BSBS**; a largely red-shifted absorption with an on-set of 396 nm (E_g = 3.13 eV, Fig. 2a) and two irreversible oxidation peaks were observed in CV, where the onset of the first oxidation peak is 0.44 V, corresponding to a HOMO level of −5.24 eV, which is markedly higher than those of **BTBT** and **BSBS**. Table 1 summarizes the energy levels and optical bandgaps of BXBXs.

These empirical electronic properties can be qualitatively reproduced by the theoretical calculations (Fig. S2, ESI†); for example, the HOMO energy levels are calculated to be −5.79, −5.51, and −5.37 eV for **BTBT**, **BSBS**, and **BTeBTe**, respectively. From the experimental results, it is obvious that the substitution of the selenium in **BSBS** with tellurium atoms yields more pronounced effects on the molecular electronic properties than the substitution of the sulphur in **BTBT** with selenium atoms. In particular, the rise of the HOMO energy level is remarkable for **BTeBTe**. This can be explained by the theoretical calculations; in the calculated distribution of HOMO coefficients of **BTeBTe**, contribution of the tellurium atoms is very large; the coefficients

Table 1 Summarized energy levels and optical bandgaps of the BXBXs

Compound	E_{onset}^{OX} [a]/V	HOMO[b]/eV	LUMO[c]/eV	E_g [d]/eV
BTBT	0.93	−5.73	−2.10	3.63
BSBS	0.80	−5.60	−2.12	3.48
BTeBTe	0.44	−5.24	−2.11	3.13

[a] *Versus* Fc/Fc$^+$. [b] Determined from the equation HOMO = −4.80 − E_{onset}^{OX}. [c] Determined from the equation LUMO = HOMO + E_g. [d] Determined from the equation E_g = 1240/(onset of absorption).

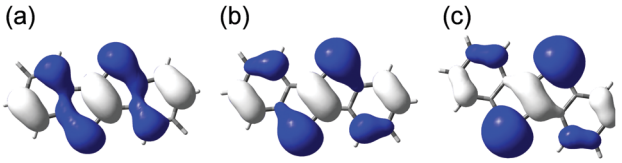

Fig. 3 The HOMO of (a) **BTBT**, (b) **BSBS** and (c) **BTeBTe** calculated at the B3LYP/3-21g level.

are localized on the tellurium atoms, implying that the nature of **BTeBTe**'s HOMO is largely affected by the tellurium atoms (Fig. 3). This is consistent with the lowest aromatic stabilization of tellurophene among the three chalcogenophenes (thiophene, selenophene and tellurophene);[38] the aromatic character of the tellurophene ring in **BTeBTe** could marginally contribute to a total stabilization in the four fused-aromatic system, which contrasts with the corresponding thiophene and selenophene rings in the **BTBT** and **BSBS** frameworks (Fig. S9, ESI†).

Packing structures in single crystals

The single-crystal structures of **BTBT**[6,39] and **BSBS**[20] have already been reported. As shown in Fig. 4a and b, **BTBT** and **BSBS** are of isostructure with a typical herringbone packing with a monoclinic $P2_1/c$ space group. The distances between the centroids in the edge-to-face and edge-to-edge dimers are 5.01 and 5.89 Å in **BTBT** and 5.18 and 6.03 Å in **BSBS**, respectively. The dihedral angles between the edge-to-face dimers are 58.08° for **BTBT** and 62.09° for **BSBS**, respectively. These marginal differences in the single-crystal structures of **BTBT** and **BSBS** suggest that the substitution of the sulphur with selenium atoms has minute influence on the molecular organization in the solid state.

In sharp contrast to the substitution of the sulphur with selenium atoms, the substitution with tellurium atoms drastically alters the packing structure. **BTeBTe** shows a dimeric herringbone packing with a monoclinic $P2_1/c$ space group (Fig. 4c). Within the dimer, the molecules are parallel with large displacement mainly along the molecular long-axis. Between the dimers, the molecules show slipped edge-to-face organization.

The fact that only the tellurium analogue, **BTeBTe**, crystalizes into a different packing structure from those of the sulphur and selenium analogues (**BTBT**/**BSBS**) contrasts with another chalcogenophene-containing system, benzo[1,2-*b*:4,5-*b*′]dichalcogenophenes, where all the sulphur, selenium, and tellurium analogues crystalize into the same herringbone packing.[40] Different trends in these systems imply that the position of the chalcogen atoms in the molecular backbone plays an important role in defining the packing structure in the solid state (*vide infra*).

Single-crystal OFETs

One of the practical reasons why the carrier transport properties of parent BXBXs have never been reported is that uniform thin films of these materials cannot be formed by the ordinary vacuum deposition. In our experiments, the vacuum deposition of **BTBT** and **BSBS** did not afford continuous thin films on the substrates. **BTeBTe** was successfully deposited on the substrates, but the thin films were almost amorphous and discontinuous, and

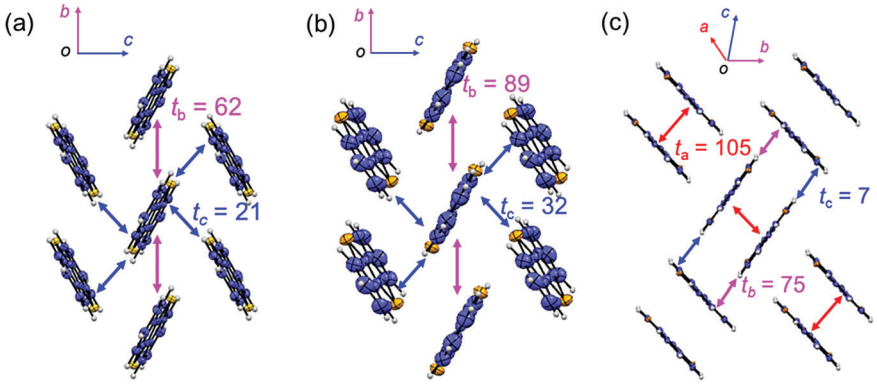

Fig. 4 Packing structures and intermolecular electronic couplings in the crystals of (a) **BTBT**, (b) **BSBS**, and (c) **BTeBTe**. The molecules are projected along the molecular long-axis direction. The non-hydrogen atoms are displayed in the ellipsoid plot with 50% probability.

accordingly not suitable as the active channel for OFETs (Fig. S5, ESI†). Thus, SC-OFETs should be the choice for investigating the carrier transport properties of BXBXs. In addition, the SC-OFETs can minimize detrimental factors that hinder the carrier transport, *i.e.*, grain boundaries and disordered packing, and thus the devices well reveal the intrinsic electronic properties of the materials.

The free-standing thin platelet crystals of BXBXs were successfully obtained through the PVT technique. The single crystals laminated on the substrates were characterized by out-of-plane X-ray diffraction (XRD). The XRD patterns of the BXBX single crystals on the substrate consist of only *h*00 peaks, judging from the powder patterns simulated from the single crystal data (Fig. S6, ESI†), indicating that the crystallographic *a*-axes are in the out-of-plane direction. This corresponds to the end-on molecular orientation on the substrates, and the crystallographic *bc* plane is parallel to the substrate for all the BXBX crystals (Fig. 4).

The carrier transport channels of the BXBXs were determined based on the facet angles of the single crystals. In the **BTBT** and **BSBS** single crystals, the molecules with the edge-to-edge molecular organization, in other words, the crystallographic *b*-axis, give the most efficient orbital overlaps (Fig. 4, see also the Discussion section), and thus this direction was selected as the FET channel in the SC-OFETs. The **BTBT** and **BSBS** single crystals exhibited similar facet angles with 108° corresponding to the dihedral angles of 011 and 0–11 directions (Fig. S7, ESI†). Thus, the bisector direction of this facet angle was determined to be the edge-to-edge direction. In the **BTeBTe** single crystals, the most efficient carrier transport direction should be along the orthogonally packed dimer molecules. The facet angle with 118° corresponds to the dihedral angles of 01–1 and 011 directions (Fig. S7, ESI†). Therefore, the facet edge direction was selected as the channel in the **BTeBTe**-based SC-OFETs.

We noticed that thermal deposition of the gold source and drain electrodes on top of the crystals caused serious damages to the single crystals of BXBXs due to a large amount of heat during the deposition process. Instead, colloidal graphite was painted as the source and drain electrodes, which turned out not to cause any damage to the single crystals.[26] The single crystals of BXBXs prepared by the PVT method have a thickness of 300–500 nm. With such thin platelet single crystals, SC-OFETs with the BGTC device configuration were fabricated (Fig. S1, ESI†). As shown in Fig. 5, the BGTC SC-OFETs based on **BTBT** and **BSBS** exhibited typical transistor characteristics. The former showed mobilities of up to 0.36 $cm^2\ V^{-1}\ s^{-1}$ (average: 0.24 $cm^2\ V^{-1}\ s^{-1}$). The mobilities extracted from the **BSBS** based devices were up to 0.90 $cm^2\ V^{-1}\ s^{-1}$ (average: 0.70 $cm^2\ V^{-1}\ s^{-1}$), which is approximately 3 times higher than those of the **BTBT**-based ones. The devices with a **BTeBTe** single crystal did not show any transistor responses.

The TGTC SC-OFETs (Fig. S1, ESI†) were also fabricated to examine the effect of device configurations on the device characteristics. As shown in Fig. S8 (ESI†), the TGTC SC-OFETs based on **BTBT** and **BSBS** exhibited typical transistor characteristics. The **BTBT** devices showed mobilities of up to 0.041 $cm^2\ V^{-1}\ s^{-1}$ (average: 0.027 $cm^2\ V^{-1}\ s^{-1}$), which is around one order of magnitude lower than those of the corresponding BGTC devices. Similarly, the mobilities of the **BSBS** devices were up to 0.13 $cm^2\ V^{-1}\ s^{-1}$ (average: 0.097 $cm^2\ V^{-1}\ s^{-1}$), which is about 8 times lower than those of the corresponding BGTC devices, but around 4 times higher than those of the **BTBT**-based TGTC devices. The **BTeBTe**-based devices again did not show any transistor responses. Table 2 summarizes the device characteristics of the SC-OFETs of **BTBT** and **BSBS**.

Evaluation of the carrier transport properties of BXBX single crystals with two different device configurations gives us several pieces of important information. First, the BGTC devices always afforded better device performances than the TGTC ones. One of the possible reasons for this is poor injection characteristics of TGTC devices (see the output characteristics in Fig. S8, ESI†), which can affect the overall device performances. The reasons for this injection issue are not clear, but we can conclude that the BGTC device configuration is more suitable to characterize the carrier transport properties of **BTBT** and **BSBS**. Second, although the mobilities obtained from the **BTBT** and **BSBS** devices are not comparable with the ones from the state-of-the-art materials with largely π-extended systems, their performances are reasonably high for the small π-conjugated system with four fused aromatic rings. Third, regardless of the device configurations, **BSBS** single crystals always showed higher mobilities than **BTBT** (3 times higher in BGTC SC-OFETs and 4 times in TGTC

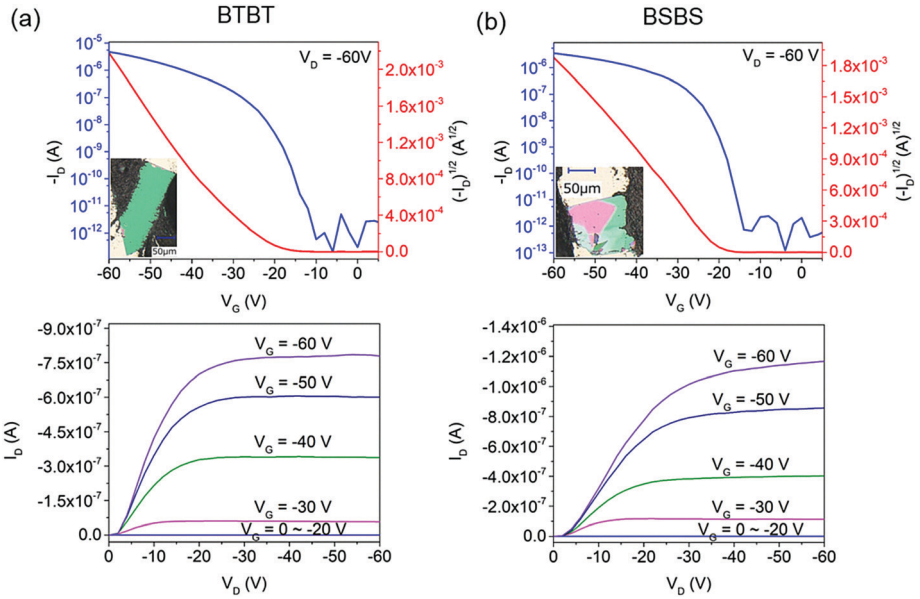

Fig. 5 Transfer (top) and output (bottom) curves of the BGTC–SC-OFETs based on (a) **BTBT** and (b) **BSBS**.

Table 2 Device characteristics of the **BTBT**/**BSBS**-based SC-OFETs

Compound	Mobility[a]/cm^2 V^{-1} s^{-1}	V_{th}/V	On/off ratio
BTBT	0.24 (0.36)[b]	−27.8[b]	10^6–10^7 [b]
	0.027 (0.041)[c]	−14.7[c]	10^4–10^5 [c]
BSBS	0.70 (0.90)[b]	−23.0[b]	10^6–10^7 [b]
	0.097 (0.13)[c]	−1.4[c]	10^4–10^5 [c]

[a] The average mobilities are based on more than 10 devices, and values in parentheses are the highest mobilities. [b] BGTC SC-OFETs. [c] TGTC SC-OFETs.

SC-OFETs, respectively), clearly indicating that the carrier transport in **BSBS** is more efficient than that in **BTBT**. Finally, even with different device configurations, the single crystals of **BTeBTe** did not act as a transistor channel, implying that the **BTeBTe** crystals could not be intrinsically suitable for transistor applications (*vide infra*).

Discussion

Effect of chalcogen atoms on intermolecular contacts in the solid state: Hirshfeld surface analysis

As discussed already, the effect of chalcogen atoms in the BXBX core on the packing structure is remarkable; in particular, the incorporation of tellurium atoms brings drastic changes in the packing structure. This implies that the chalcogen atoms can alter the intermolecular contacts in the solid state. Hirshfeld surface analysis, an effective measure to visualize intermolecular contacts, was thus carried out. As shown in Fig. 6a, the Hirshfeld surface of **BTBT** mapped with d_e (distance from the surface to the nearest nucleus external to the surface) exhibits intermolecular contacts along the molecular edge and π-faces (large green and red regions on the surface). The ratio of these intermolecular contacts (*i.e.*, C–H and S–C contacts) comprises more than 50% (Fig. S10, ESI†) of the total intermolecular contacts, suggesting that the edge-to-face intermolecular interaction contributes to stabilize the herringbone packing of **BTBT**. This is further confirmed by the calculations of intermolecular interaction energies (Table S1, ESI†) in the edge-to-face and edge-to-edge dimers by the SAPT method. The intermolecular interaction energy of the edge-to-face dimer is −11.24 kcal mol^{-1}, and this is approximately 1.4 times larger than that of the edge-to-edge dimer (−8.35 kcal mol^{-1}), in which the dispersion gives the largest contribution (−15.03 kcal mol^{-1} for the edge-to-face dimer and −10.89 kcal mol^{-1} for the edge-to-edge dimer, respectively).

From these analyses, the herringbone packing of **BTBT** is concluded to be a dispersion-driven packing structure that is facilitated by the edge-to-face CH–π contacts similar to the acenes and other thienoacenes.[41] The results of Hirshfeld surface analysis as well as the SAPT calculations of **BSBS** are basically the same as those of **BTBT**, in terms of the distribution and ratio of each intermolecular contact and energetical stabilization (Fig. 6b and Fig. S10, ESI†).

The Hirshfeld surface of **BTeBTe** is significantly different from those of **BTBT** and **BSBS** (Fig. 6c and d). Although similar edge-to-face CH–π contacts between the hydrogen atoms in the benzene rings and the π-surface are observed, only part of the molecular edges are involved in the contacts. This is obviously owing to the existence of tellurium atoms in the middle of the molecule. In other words, because of the large atomic radius and elongated C–Te bonds, the tellurium atoms in the **BTeBTe** core protrude at the molecular edges, resulting in the whole molecular edges unavailable for the edge-to-face CH–π contacts that play the key role in the formation of the herringbone packing structure. In addition, the incorporation of tellurium atoms makes the molecular shape rather "square-like" (Fig. 6c and d), which contrasts with the rectangular-shaped **BTBT** and **BSBS** (Fig. 6a and b). As two-dimensional extension of π-conjugated systems often makes the π–π stacking structure favourable,[42,43]

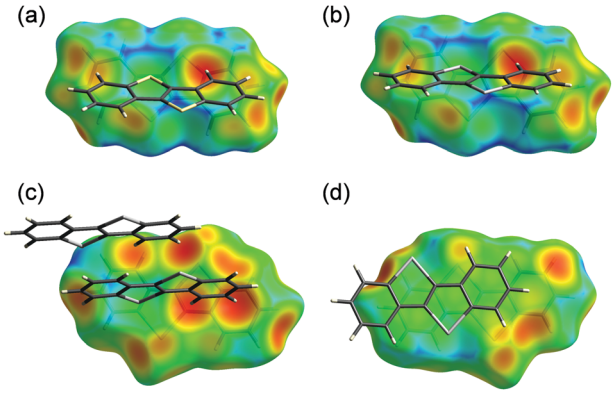

Fig. 6 Hirshfeld surface and ratio of intermolecular short contacts of the BXBX molecules extracted from the respective crystal structures mapped with d_e: (a) **BTBT**, (b) **BSBS**, and (c and d) **BTeBTe** for the CH–π side and π–π side.

the co-facial dimer of **BTeBTe** can be rationally explained. Because of such a characteristic molecular shape of **BTeBTe**, the ratio of C–H contact is decreased (Fig. S10, ESI†), and instead the intermolecular contacts including the tellurium atoms, *i.e.*, Te–H and Te–C, increase significantly, more than 30% for **BTeBTe**, whereas *ca.* 25 (26)% of S (Se)–H and S (Se)–C for **BTBT** (**BSBS**). We can thus conclude that the molecular shape of **BTeBTe** changes the intermolecular interaction and thereby the packing structure. This, in turn, is regarded as a significant "heavy-atom effect" caused by the tellurium atoms in the BXBX core. In fact, substitution of one sulphur atom in **BTBT** with a tellurium atom, *e.g.*, [1]benzotelluropheno[3,2-*b*][1]benzothiophene, has a similar dimeric herringbone packing to **BTeBTe**.[44]

Effect of chalcogen atoms on intermolecular electronic coupling in the solid state and transport properties

BTBT and BSBS. **BTBT** shows typical anisotropic orbital overlaps with moderately large electronic coupling (t). The t along the edge-to-edge direction (crystallographic *b*-axis, t_b) is 62 meV, and that along the edge-to-face direction (t_a) is 21 meV (Fig. 4a). A similar anisotropic electronic coupling to **BTBT** is observed in **BSBS**. The t values along the edge-to-edge (crystallographic *b*-axis, t_b: 89 meV) and edge-to-face (t_c: 32 meV) directions are about 1.5 times larger than the corresponding ones in **BTBT**. The remarkable increase of t_s in **BSBS** could be regarded as a positive "heavy-atom effect", *i.e.*, enhanced electronic coupling between neighbouring molecules thanks to the larger atomic radius and more diffused electron clouds of selenium than sulphur atoms. This is reasonably consistent with the higher mobilities of the **BSBS**-based SC-OFETs than the **BTBT** counterpart.

To get further insight into the carrier transport properties of parent **BTBT** and **BSBS**, their theoretical anisotropic mobilities under the ideal environment are simulated in the hopping regime by utilizing the Marcus/Hush model.[30,45] As **BTBT** and **BSBS** form lamellar structures in the single crystals and adopt the end-on molecular orientation on the substrate, the crystallographic *bc* plane should be considered as the conducting layer.[31] Inside the conducting layer, the carrier transport can be determined by combining the electronic couplings from all the hopping pathways. The anisotropic mobilities were calculated with the *b*-axis direction as the reference axis (Fig. S11, see ESI† for details).

The key parameters dictating the carrier mobility in the hopping regime are t (Fig. 4) and reorganization energy (λ). The λ_s values of **BTBT** and **BSBS** are calculated to be 225 and 198 meV, respectively. The lower λ of **BSBS** than **BTBT** can be explained by the more diffused molecular orbitals of **BSBS** than **BTBT** thanks to the selenium atoms, which makes the radical cations of **BSBS** less deformed during the carrier transport. The theoretical mobilities of **BTBT** are calculated to be 0.01 (along the *c*-axis) – 0.85 (along the *b*-axis) $cm^2\ V^{-1}\ s^{-1}$, and those of **BSBS** are in the range of 0.04 (along the *c*-axis) – 2.47 (along the *b*-axis) $cm^2\ V^{-1}\ s^{-1}$ (Fig. 7). Since the difference in λ between **BTBT** and **BSBS** is not that large, the higher mobilities of **BSBS** are mainly attributed to their larger intermolecular electronic coupling than **BTBT**. The theoretical calculations indicate that the substitution of the sulphur with selenium atoms does improve the carrier transport properties mainly by enhancing the intermolecular electronic coupling. The increasing trend of the theoretical mobilities is well consistent with the empirical results (Table 2). On the other hand, the theoretical mobilities are approximately 3 times higher than the experimental values, implying that the SC-OFETs still have some room for improvement.

BTeBTe. The **BTBT**–**BSBS** system is regarded as an ideal case for the positive "heavy-atom effect" in organic semiconductors, where the heavy atom, *i.e.*, selenium, does contribute to enhance the intermolecular electronic coupling and thereby transport properties in the solid state. **BTeBTe**, on the other hand, is not on the same line as such an ideal case, because of the drastic change in the packing structure from the herringbone to dimeric herringbone packing (Fig. 4c). However, the change in the packing structure cannot solely explain why the **BTeBTe**-based SC-OFET did not show any transistor characteristics. To clarify this, we first looked at the intermolecular electronic coupling in the crystal structure of **BTeBTe**.

As shown in Fig. 4c, the intermolecular electronic coupling within the **BTeBTe** dimers is as large as 105 meV (t_a). Since there is certain displacement along the long molecular axis in the dimers, the intermolecular electronic couplings between the molecules in the neighbouring dimers are inequivalent.

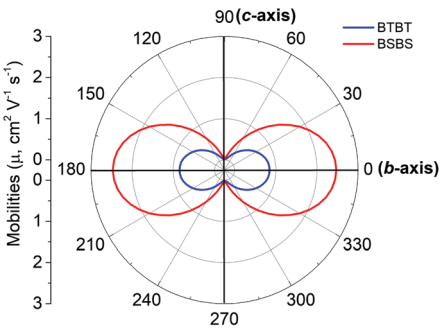

Fig. 7 Calculated anisotropic mobilities in the ideal **BTBT** and **BSBS** crystals (the 0° and 180° directions are along the edge-to-edge direction (crystallographic *b*-axis) for **BTBT** and **BSBS**; see also Fig. S11, ESI†).

The less displaced molecules in the neighbouring dimers yield a fairly large t (t_b, 75 meV), and in contrast, t_c for the largely displaced molecule is only 7 meV. It seems that the large t in the dimer locally facilitates the carrier transport, but the overall transport is affected by the intermolecular electronic coupling in all the directions including the ones with very poor electronic coupling (t_c, 7 meV). In other words, this ineffective path might be the bottleneck of carrier transport in the *bc* conducting plane. However, this does not reasonably explain why the **BTeBTe** based SC-OFETs showed no transistor responses. In fact, a similar dimeric herringbone structure was reported for dinaphtho[1,2-*b*:1′,2′-*f*]thieno[3,2-*b*]thiophene, the thin-film transistors of which show decent transistor characteristics with mobilities of up to 10^{-2} cm^2 V^{-1} s^{-1}.[46]

In order to get further insight into **BTeBTe**, two additional analyses were carried out. One is to evaluate the ionization potential (IP) of the solid samples of **BTeBTe** (Fig. S12, ESI†) by means of photoelectron spectroscopy in air to confirm the efficiency of hole injection from the electrode into the SC-OFETs. IPs of **BTBT**, **BSBS** and **BTeBTe** were thus experimentally determined to be 5.8, 5.6 and 5.4 eV, which are mostly consistent with their electrochemically determined HOMO energy levels (Table 1). This means that the hole injection from the electrode should be better in the **BTeBTe**-based SC-OFETs than in the **BTBT**- and **BSBS**-based ones, which can rule out the hole injection issue from the possible causes that make the **BTeBTe**-based SC-OFETs show no transistor response.

The other is to calculate the band structure of **BTeBTe** together with **BTBT** and **BSBS**, instead of the calculation of anisotropic mobilities, since the latter method is not applicable to **BTeBTe** with the dimeric herringbone structure owing to indeterminable hopping pathways. As depicted in Fig. 8 and Fig. S13 (ESI†), the calculated band structures of **BTBT** and **BSBS** have a similar dispersion, where the bandwidth of the Γ–Y direction, which corresponds to the crystallographic *b*-axis, is larger than that of the Γ–Z direction (crystallographic *c*-axis), consistent with the anisotropy of electronic couplings of the HOMO (Fig. 4a and b). For **BSBS**, the bandwidth in the Γ–Y direction is as large as 481 meV, which is approximately 1.6 times larger than that of **BTBT** (292 meV). In contrast, the band dispersion of **BTeBTe** is different from those of **BTBT** and **BSBS** reflected by the dimeric herringbone structure, and the largest bandwidth of 243 meV is calculated for the Γ–Y direction. Although the smallest bandwidth of **BTeBTe** among the three compounds is reasonable for the strong dimerization of molecules, it could not directly rationalize the silent behaviours of the **BTeBTe**-based SC-OFETs. Furthermore, effective carrier masses (m^*) in the Γ–Y direction were estimated by parabolic-fitting at the band extrema (Fig. S14, ESI†), and the extracted m^*s values were 0.73, 0.44, and 0.52 for **BTBT**, **BSBS**, and **BTeBTe**, respectively. This strongly implies that the dimeric herringbone structure is not the detrimental factor for effective carrier transport.

Even with these two additional analyses on the solid-state properties, we could not find the rationale for the device behaviour of **BTeBTe**. We thus turned our attention once again to molecular electronic structures. As already pointed out, **BTeBTe** has distinct molecular electronic properties among the BXBX system, which can be boiled down to the significant contribution of the tellurium atoms to the electronic structure of **BTeBTe** (Fig. 3). For the p-type organic semiconductors, the nature of the HOMO is critically important, and in this regard, the fact that the HOMO coefficients strongly localized on the tellurium atoms could not be desirable for efficient carrier transport in the solid state, because the injected holes from the electrode tend to localize on the particular part of the molecules. In fact, the spin density calculated for the **BTeBTe** radical cation shows significant localization of spin on the tellurium

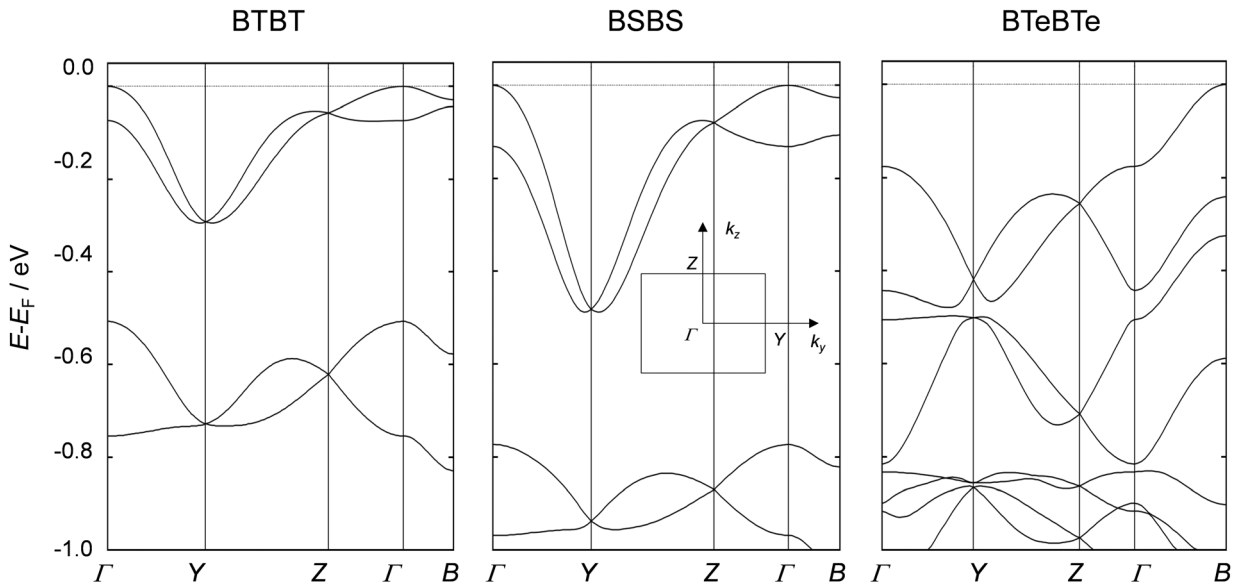

Fig. 8 The DFT-calculated band structures of **BTBT**, **BSBS**, and **BTeBTe**. The reciprocal coordinates of the high-symmetry points are Γ = (0 0 0), Y = (0 1/2 0), Z = (0 0 1/2), and B = (1/2 0 0). Note that only several valence bands just below the Fermi level are shown to clarify the differences between the band structures that closely relate to the hole transport. The inset represents the Brillouin zone diagram with respect to the crystallographic cell.

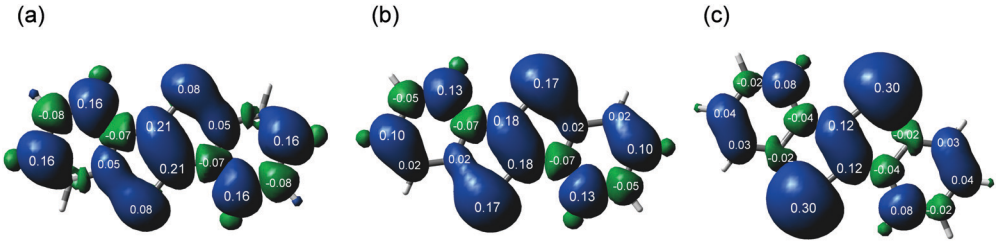

Fig. 9 Distribution of spin density in the radical cationic state of (a) **BTBT**, (b) **BSBS** and (c) **BTeBTe**. The numbers on the atoms are the ratios of spins.

atoms (Fig. 9c), approximately 60% spin density on the tellurium atoms. Furthermore, more than 80% spin density is localized on the central ditelluraethene (C_2Te_2) moiety, and the outermost benzene rings poorly contribute to spin delocalization. In sharp contrast, the spin density in **BTBT**- and **BSBS**-radical cations is delocalized over the π-framework (Fig. 9a and b). The localized spin on the tellurium atoms in **BTeBTe** tends to be less mobile in the solid state than the delocalized spin in **BTBT** and **BSBS**, implying that the nature of active carrier species in the working devices is affected by the chalcogen atoms in the molecular framework. Although we cannot conclude that the strong localization nature of spin in the **BTeBTe** radical cation is the actual cause for the silent FET behaviour, the tellurium atoms in the BXBX core could alter the nature of molecules in both the neutral and charged states, which can largely affect the mobility of active carriers in the crystal of **BTeBTe**.

Conclusions

The concept of ''heavy-atom effects'' has been regarded as an effective measure to improve the carrier mobility of organic semiconductors, since the carrier transport in organic semiconducting solids is governed by intermolecular orbital overlap, which can be enhanced by using ''heavy'' chalcogen atoms such as selenium and tellurium instead of sulphur atoms. With the parent BXBX system, we have tried to verify the concept by elucidating the molecular electronic structures, packing structures and intermolecular interaction in the solid state, the solid-state electronic structures, and carrier transport properties.

The substitution of the sulphur in **BTBT** with selenium atoms only slightly alters the molecular electronic properties and the packing structure, and thereby the electronic structures at the solid state are very similar to each other. As a result of the larger atomic radius and more diffused electron density of selenium than sulphur atoms, the intermolecular electronic coupling in **BSBS** is enhanced, which results in improved carrier mobility in the SC-OFETs of **BSBS**. This can be regarded as a positive side of the ''heavy-atom effect''. On the other hand, the substitution of the selenium in **BSBS** with tellurium atoms significantly changes not only the molecular electronic properties but also the packing structures. These significant changes can be explained by the nature of tellurium atoms in the π-conjugated framework, poor conjugation in the π-system and low aromaticity of the tellurophene moiety, and the elongated C–Te bonds that distort a whole molecular structure. Consequently, the solid-state electronic structure of **BTeBTe** is significantly different from those of **BTBT** and **BSBS**. Furthermore it is somewhat surprising that the **BTeBTe**-based SC-OFETs show no transistor responses. Although we cannot completely figure out the actual cause of the silent behaviours of the **BTeBTe** SC-OFETs, several distinctive features of **BTeBTe** as an organic semiconductor, such as a high-lying HOMO energy level, significant contribution of tellurium atoms to the molecular electronic structure both at the neutral and radical cation states, and the dimeric herringbone structure with a relatively narrow HOMO band, are elucidated. These features may not be always positive in the application of **BTeBTe** to the FET channel. We believe, however, that to understand these distinctive features of tellurium-containing molecules could be useful in developing organic semiconductors in future.

Conflicts of interest

There are no conflicts to declare.

Acknowledgements

We thank Dr Daisuke Hashizume in RIKEN for his help in solving the crystal structure of **BTeBTe**. We thank Dr Lionel Hirsch and Marco Pereira in Univ. Bordeaux, IMS, CNRS, for their assistance in the fabrication of SC-OFETs. We thank the Super-computer System in the Advanced Center for Computing and Communication (ACCC) of RIKEN and the Center for Computational Materials Science, Institute for Materials Research, Tohoku University, for the use of MASAMUNE-IMR (MAterials science Supercomputing system for Advanced MUlti-scale simulations towards NExt-generation – Institute for Materials Research) for support in theoretical calculations. This work was financially supported by JSPS KAKENHI Grant Numbers JP15H02196 and JP19H00906, and the Bilateral Programs between Japan and France supported by JSPS and CNRS.

Notes and references

1 C. Wang, H. Dong, W. Hu, Y. Liu and D. Zhu, *Chem. Rev.*, 2012, **112**, 2208–2267.
2 H. Dong, X. Fu, J. Liu, Z. Wang and W. Hu, *Adv. Mater.*, 2013, **25**, 6158–6183.
3 H. Sirringhaus, *Adv. Mater.*, 2014, **26**, 1319–1335.
4 J. E. Anthony, *Chem. Rev.*, 2006, **106**, 5028–5048.
5 K. Takimiya, S. Shinamura, I. Osaka and E. Miyazaki, *Adv. Mater.*, 2011, **23**, 4347–4370.

6 K. Takimiya, I. Osaka, T. Mori and M. Nakano, *Acc. Chem. Res.*, 2014, **47**, 1493–1502.
7 K. Takimiya, H. Ebata, K. Sakamoto, T. Izawa, T. Otsubo and Y. Kunugi, *J. Am. Chem. Soc.*, 2006, **128**, 12604–12605.
8 H. Ebata, T. Izawa, E. Miyazaki, K. Takimiya, M. Ikeda, H. Kuwabara and T. Yui, *J. Am. Chem. Soc.*, 2007, **129**, 15732–15733.
9 H. Iino, T. Usui and J.-I. Hanna, *Nat. Commun.*, 2015, **6**, 6828.
10 H. Minemawari, M. Tanaka, S. Tsuzuki, S. Inoue, T. Yamada, R. Kumai, Y. Shimoi and T. Hasegawa, *Chem. Mater.*, 2017, **29**, 1245–1254.
11 T. Yamamoto and K. Takimiya, *J. Am. Chem. Soc.*, 2007, **129**, 2224–2225.
12 K. Niimi, S. Shinamura, I. Osaka, E. Miyazaki and K. Takimiya, *J. Am. Chem. Soc.*, 2011, **133**, 8732–8739.
13 H. Minemawari, T. Yamada, H. Matsui, J. Y. Tsutsumi, S. Haas, R. Chiba, R. Kumai and T. Hasegawa, *Nature*, 2011, **475**, 364–367.
14 Y. Yuan, G. Giri, A. L. Ayzner, A. P. Zoombelt, S. C. B. Mannsfeld, J. Chen, D. Nordlund, M. F. Toney, J. Huang and Z. Bao, *Nat. Commun.*, 2014, **5**, 3005.
15 X. Liu, X. Su, C. Livache, L.-M. Chamoreau, S. Sanaur, L. Sosa-Vargas, J.-C. Ribierre, D. Kreher, E. Lhuillier, E. Lacaze and F. Mathevet, *Org. Electron.*, 2020, **78**, 105605.
16 Y. Kunugi, K. Takimiya, K. Yamane, K. Yamashita, Y. Aso and T. Otsubo, *Chem. Mater.*, 2003, **15**, 6–7.
17 A. Patra and M. Bendikov, *J. Mater. Chem.*, 2010, **20**, 422–433.
18 A. A. Jahnke and D. S. Seferos, *Macromol. Rapid Commun.*, 2011, **32**, 943–951.
19 E. I. Carrera and D. S. Seferos, *Macromolecules*, 2015, **48**, 297–308.
20 K. Takimiya, Y. Kunugi, Y. Konda, H. Ebata, Y. Toyoshima and T. Otsubo, *J. Am. Chem. Soc.*, 2006, **128**, 3044–3050.
21 T. Izawa, E. Miyazaki and K. Takimiya, *Chem. Mater.*, 2009, **21**, 903–912.
22 H. Sugino and K. Takimiya, *Chem. Lett.*, 2017, **46**, 345–347.
23 M. Saito, I. Osaka, E. Miyazaki, K. Takimiya, H. Kuwabara and M. Ikeda, *Tetrahedron Lett.*, 2011, **52**, 285–288.
24 H. Sashida and S. Yasuike, *J. Heterocycl. Chem.*, 1998, **35**, 725–726.
25 R. A. Laudise, C. Kloc, P. G. Simpkins and T. Siegrist, *J. Cryst. Growth*, 1998, **187**, 449–454.
26 R. Zeis, T. Siegrist and C. Kloc, *Appl. Phys. Lett.*, 2005, **86**, 022103.
27 M. J. Frisch, G. W. Trucks, H. B. Schlegel, G. E. Scuseria, M. A. Robb, J. R. Cheeseman, G. Scalmani, V. Barone, G. A. Petersson, H. Nakatsuji, X. Li, M. Caricato, A. V. Marenich, J. Bloino, B. G. Janesko, R. Gomperts, B. Mennucci, H. P. Hratchian, J. V. Ortiz, A. F. Izmaylov, J. L. Sonnenberg, D. Williams-Young, F. Ding, F. Lipparini, F. Egidi, J. Goings, B. Peng, A. Petrone, T. Henderson, D. Ranasinghe, V. G. Zakrzewski, J. Gao, N. Rega, G. Zheng, W. Liang, M. Hada, M. Ehara, K. Toyota, R. Fukuda, J. Hasegawa, M. Ishida, T. Nakajima, Y. Honda, O. Kitao, H. Nakai, T. Vreven, K. Throssell, J. A. Montgomery, Jr., J. E. Peralta, F. Ogliaro, M. J. Bearpark, J. J. Heyd, E. N. Brothers, K. N. Kudin, V. N. Staroverov, T. A. Keith, R. Kobayashi, J. Normand, K. Raghavachari, A. P. Rendell, J. C. Burant, S. S. Iyengar, J. Tomasi, M. Cossi, J. M. Millam, M. Klene, C. Adamo, R. Cammi, J. W. Ochterski, R. L. Martin, K. Morokuma, O. Farkas, J. B. Foresman and D. J. Fox, *Gaussian 16, Revision C.01*, Gaussian, Inc., Wallingford CT, 2016.
28 G. R. Hutchison, M. A. Ratner and T. J. Marks, *J. Am. Chem. Soc.*, 2005, **127**, 2339–2350.
29 ADF: powerful DFT code for modeling molecules, Scientific Computing and Modeling, Amsterdam, http://www.scm.com/ADF/.
30 A. Troisi and G. Orlandi, *Phys. Rev. Lett.*, 2006, **96**, 086601.
31 S.-H. Wen, A. Li, J. Song, W.-Q. Deng, K.-L. Han and W. A. Goddard, *J. Phys. Chem. B*, 2009, **113**, 8813–8819.
32 J. J. McKinnon, M. A. Spackman and A. S. Mitchell, *Acta Crystallogr., Sect. B: Struct. Sci.*, 2004, **60**, 627–668.
33 M. J. Turner, J. J. McKinnon, S. K. Wolff, D. J. Grimwood, M. A. Spackman, D. Jayatilaka and M. A. Spackman, *CrystalExplorer17*, University of Western Australia, 2017, http://hirshfeldsurface.net.
34 B. Jeziorski, R. Moszynski and K. Szalewicz, *Chem. Rev.*, 1994, **94**, 1887–1930.
35 R. M. Parrish, L. A. Burns, D. G. A. Smith, A. C. Simmonett, A. E. DePrince, E. G. Hohenstein, U. Bozkaya, A. Y. Sokolov, R. Di Remigio, R. M. Richard, J. F. Gonthier, A. M. James, H. R. McAlexander, A. Kumar, M. Saitow, X. Wang, B. P. Pritchard, P. Verma, H. F. Schaefer, K. Patkowski, R. A. King, E. F. Valeev, F. A. Evangelista, J. M. Turney, T. D. Crawford and C. D. Sherrill, *J. Chem. Theory Comput.*, 2017, **13**, 3185–3197.
36 R. Dovesi, A. Erba, R. Orlando, C. M. Zicovich-Wilson, B. Civalleri, L. Maschio, M. Rérat, S. Casassa, J. Baima, S. Salustro and B. Kirtman, *Wiley Interdiscip. Rev.: Comput. Mol. Sci.*, 2018, **8**, e1360.
37 M. Z. S. Flores, V. N. Freire, R. P. dos Santos, G. A. Farias, E. W. S. Caetano, M. C. F. de Oliveira, J. R. L. Fernandez, L. M. R. Scolfaro, M. J. B. Bezerra, T. M. Oliveira, G. A. Bezerra, B. S. Cavada and H. W. Leite Alves, *Phys. Rev. B: Condens. Matter Mater. Phys.*, 2008, **77**, 115104.
38 E. Vessally, *J. Struct. Chem.*, 2008, **49**, 979–985.
39 C. Niebel, Y. Kim, C. Ruzié, J. Karpinska, B. Chattopadhyay, G. Schweicher, A. Richard, V. Lemaur, Y. Olivier, J. Cornil, A. R. Kennedy, Y. Diao, W.-Y. Lee, S. Mannsfeld, Z. Bao and Y. H. Geerts, *J. Mater. Chem. C*, 2015, **3**, 674–685.
40 K. Takimiya, Y. Konda, H. Ebata, N. Niihara and T. Otsubo, *J. Org. Chem.*, 2005, **70**, 10569–10571.
41 G. Gryn'ova and C. Corminboeuf, *J. Phys. Chem. Lett.*, 2016, **7**, 5198–5204.
42 G. R. Desiraju and A. Gavezzotti, *Acta Crystallogr., Sect. B: Struct. Sci.*, 1989, **45**, 473–482.
43 F. P. A. Fabbiani, D. R. Allan, S. Parsons and C. R. Pulham, *Acta Crystallogr., Sect. B: Struct. Sci.*, 2006, **62**, 826–842.
44 M. Matsumura, A. Muranaka, R. Kurihara, M. Kanai, K. Yoshida, N. Kakusawa, D. Hashizume, M. Uchiyama and S. Yasuike, *Tetrahedron*, 2016, **72**, 8085–8090.
45 M. Hultell and S. Stafström, *Chem. Phys. Lett.*, 2006, **428**, 446–450.
46 T. Yamamoto, S. Shinamura, E. Miyazaki and K. Takimiya, *Bull. Chem. Soc. Jpn.*, 2010, **83**, 120–130.